Nature Communications

https://doi.org/10.1038/s41467-026-72867-x

Article in Press

MOF gel network crosslinked mixed matrix membranes with engineered interface for high-efficiency Helium recovery

Received: 3 July 2025

Accepted: 24 April 2026

Cite this article as: Zhang, K., Huan, H., Tian, X. *et al.* MOF gel network crosslinked mixed matrix membranes with engineered interface for high-efficiency Helium recovery. *Nat Commun* (2026). https://doi.org/10.1038/s41467-026-72867-x

Keming Zhang, Haishan Huan, Xiaohe Tian, Chongshan Yin, Xiaohua Ma & Shaofei Wang

MOF Gel Network Crosslinked Mixed Matrix Membranes with Engineered Interface for High-Efficiency Helium Recovery

Keming Zhang[1,4], Haishan Huan[1,4], Xiaohe Tian[1,4], Chongshan Yin[2], Xiaohua Ma[3], Shaofei Wang[1,4]**

[1] State Key Laboratory of Chemo and Biosensing, College of Chemistry and Chemical Engineering, Hunan University, Changsha 410082, China.

[2] Hunan Provincial Key Laboratory of Flexible Electronic Materials Genome Engineering, School of Physics and Electronic Science, Changsha University of Science and Technology, Changsha 410114, China.

[3] State Key Laboratory of Separation Membranes and Membrane Processes, School of Materials Science and Engineering, Tiangong University, Tianjin, 300387, China.

[4] Greater Bay Area Institute for Innovation, Hunan University, Guangzhou 511340, China.

** Corresponding author: shaofeiwang@hnu.edu.cn, xhuama@tiangong.edu.cn*

Abstract: Helium (He) recovery via conventional cryogenic distillation is highly energy-intensive and costly. Membrane separation features modularity and efficiency, but mixed-matrix membranes (MMMs) often suffer from discontinuous channels and poor filler–polymer compatibility, which impair separation performance. Here, we report an MMM platform by embedding a continuous 3D nanoporous ZIF-67-NH_2 gel within a polyimide matrix. The gel functions as a dual-functional crosslinker, forming covalent amide linkages and hydrogen bonds with the polymer to eliminate interfacial voids, while creating interconnected, selective nanochannels through its intrinsic nanoporosity. This yields He/CH_4 performance: 549 Barrer He permeability and 110.3 selectivity, surpassing the benchmark membranes. The membrane retains over 95% performance in mixed-gas tests over 180 h. Process simulations show that a hybrid membrane – cryogenic system achieves >93% He recovery and 74% energy savings. This work provides an energy-efficient platform for critical gas separations.

1 Introduction

Helium (He), a non-renewable noble gas vital for aerospace, cryogenics, and semiconductors[1, 2, 3, 4, 5] has an atmospheric abundance of only 5 ppm, driving demand for efficient recovery[6]. Conventional cryogenic distillation is energy-intensive and capital-intensive, resulting in high operational and investment costs[7]. These drawbacks have spurred growing interest in membrane-based separations, which offer advantages such as lower energy consumption and modular scalability. However, achieving both high permeability and selectivity for He/CH_4 separations remains challenging.

Compared to conventional cryogenic processes, membrane-based separation offers distinct advantages for helium recovery: modular design, simple operation, and notably lower energy consumption[8, 9, 10, 11, 12, 13]. Nevertheless, these technologies still face significant obstacles. Conventional polymer membranes are constrained by the permeability–selectivity trade-off[14, 15]. While mixed-matrix membranes (MMMs) that embed rigid fillers to overcome this, they often face two major issues: (i) isolated particles disrupt and elongate diffusion pathways, hindering the transport of fast gases such as He[16]; and (ii) poor polymer–filler adhesion creates nanoscale voids that act as nonselective leaks, undermining separation performance[10, 17].

To address interfacial incompatibilities, researchers have explored surface functionalization—via amine grafting, dopamine coatings or ionic-liquid infusion—to enhance interfacial affinity through noncovalent forces, yet yields only modest selectivity gains (<50%)[18, 19, 20, 21, 22]. Moderate chemical crosslinking can further improve selectivity by forging covalent bonds (radical copolymerization, amine-carboxyl condensation, coordination bonding) between filler and polymer, yet the inherently weak chemistry still limits improvements to <100% enhancement[23, 24, 25, 26, 27]. Conversely, aggressive crosslinking techniques such as ethylenediamine treatment and cyano-thermal cyclization exploit the inherent size-exclusion properties of MOFs to boost selectivity by over 300%, but they often induce a severe reduction in free volume and a consequent decrease in permeability[28, 29, 30]. Consequently, achieving both high permeability and precise molecular sieving within a single MMM remains a formidable challenge.

Here, we report a dual-crosslinking MMM that integrates amino-functionalized ZIF-67-NH_2 gel into a high–free-volume 6FDA-TMPD polyimide matrix to form a continuous three-dimensional nanoporous network. In contrast to conventional crystalline MOF particles, the ZIF-67-NH_2 gel exhibits an interconnected architecture with pore apertures around 0.34 nm, which closely match the kinetic diameter gap between He (0.26 nm) and CH_4 (0.38 nm). This structural continuity facilitates efficient gas transport and molecular sieving. Crucially, distinct from the physical blending paradigm, the amino-functionalization facilitates covalent crosslinking and hydrogen bonding with the polymer matrix, resulting in significantly enhanced interfacial compatibility and structural integrity. By systematically tuning the filler loading and characterizing the resulting structure–property relationships, we realize a membrane that simultaneously delivers high helium permeability and He/CH_4 selectivity, outperforming the traditional Robeson bound. Moreover, long-duration testing under simulated industrially relevant conditions confirms stable operation, and process simulations highlight a marked reduction in energy demand and capital expenditure for large-scale helium recovery. Our findings showcase how rational interfacial engineering of MOF-gel fillers can surmount the longstanding challenges of polymer-based MMMs, yielding defect-free membranes with enhanced He/CH_4 separation performance. This strategy offers a scalable, energy-efficient route to helium recovery and can be extended to other critical gas separations.

Results

Characterization of ZIF-67-NH_2 Gel

The ZIF-67-NH_2 gel was synthesized via a coordination-modulation–induced gelation method using a mixed-ligand strategy[16, 31, 32](Fig. 1a). In brief, $Co(NO_3)_2 \cdot 6H_2O$ and mixed ligands (2-methylimidazole:2-aminobenzimidazole, 9:1 molar ratio) were dissolved in methanol, and gelation was triggered by adding 0.8 mL of triethylamine. For comparison, unmodified ZIF-67 gels were also synthesized (Fig. 1b). Transmission electron microscopy (TEM, Fig. 1c) reveals a continuous, high-aspect-ratio network of interwoven MOF strands whose topology is similar to ZIF-67 gel (Fig. 1d). To further validate the successful synthesis of ZIF-67 gel and ZIF-67-NH_2

gel, dynamic rheological measurements were conducted. As shown in Supplementary Fig. 1, the storage modulus (G') is significantly higher than the loss modulus (G''). This result indicates that the synthesized ZIF-67 gel and ZIF-67-NH_2 gel exhibit the stability characteristic of MOF gel materials[33, 34]. This structural similarity indicates that –NH_2 functionalization does not hinder gelation, nor does it damage the three-dimensional connectivity of the gel network. Such a preserved, slender-rod framework is essential—when embedded within the polymer matrix, it establishes interconnected gas-transport channels that enhance gas separation performance in the resulting MMMs.

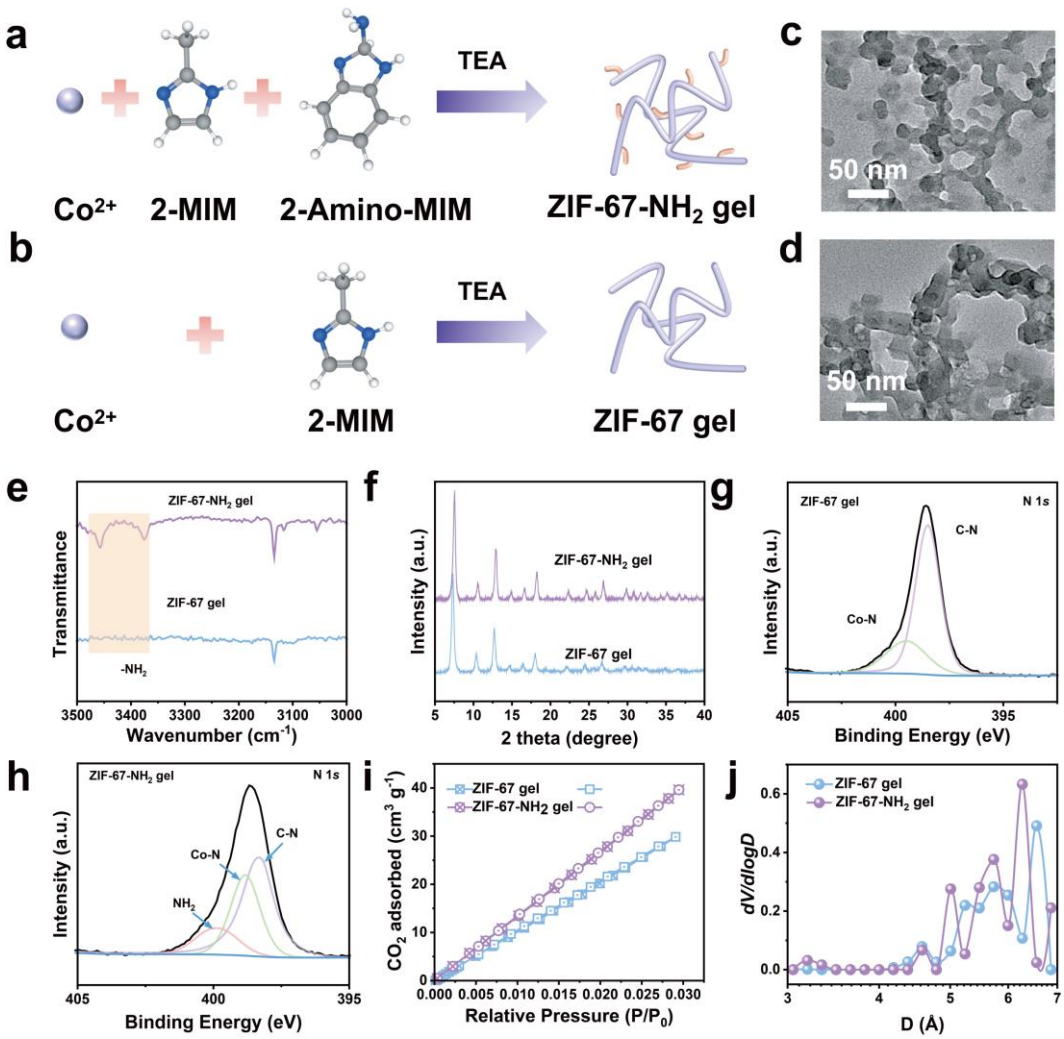

Fig. 1 Synthesis and characterization of ZIF-67-NH_2 gels and ZIF-67 gels. Schematic diagram of the synthesis of **a)** ZIF-67-NH_2 gel and **b)** ZIF-67 gel. TEM images of **c)** ZIF-67-NH_2 gel and **d)** ZIF-67 gel. **e)** FT-

IR spectra of ZIF-67-NH_2 gel and ZIF-67 gel. **f)** XRD patterns of ZIF-67-NH_2 gel and ZIF-67 gel. High-resolution N 1*s* XPS spectra of **g)** ZIF-67 gel and **h)** ZIF-67-NH_2 gel. **i)** CO_2 adsorption-desorption isotherms (273 K) of ZIF-67 gel and ZIF-67-NH_2 gel. **j)** Pore size distribution of ZIF-67-NH_2 gel and ZIF-67 gel based on non-local density functional theory using CO_2 isotherms.

To further elucidate the effects of amino functionalization on the structure, both ZIF-67-NH_2 and the unmodified ZIF-67 gels were subjected to comprehensive characterization using X-ray diffraction (XRD), Fourier transform infrared (FT-IR) spectroscopy, X-ray photoelectron spectroscopy (XPS), and ^{1}H nuclear magnetic resonance (^{1}H NMR) spectroscopy. The corresponding results are depicted in Fig. 1e–h and Supplementary Fig. 2 and Fig. 3. The XRD patterns (Fig. 1e) confirm that both materials share the same crystalline structure with high crystallinity. Although the amino ligand (2-aminobenzimidazole, 2-amino-MIM) is partially incorporated into the ZIF-67 framework, the overall crystallinity is well preserved. Minor peak shifts and broadening are observed in ZIF-67-NH_2, possibly indicating the presence of lattice strain or increased structural disorder due to functionalization[35]. FT-IR spectra (Fig. 1f) display notable differences between the two materials. In particular, ZIF-67-NH_2 exhibits two new absorption bands at approximately 3375 cm^{-1} and 3456 cm^{-1}, attributed to the symmetric and asymmetric stretching vibrations of the $–NH_2$ group[36], confirming the successful incorporation of amino functionalities into the MOF framework. XPS profiling supports this claim, showing a significant increase in the intensity of peaks associated with nitrogen-containing functionalities (Fig. 1g–h and Supplementary Fig. 2). To quantify the ratio of 2-aminobenzimidazole, we performed ^{1}H NMR spectroscopy. As shown in Supplementary Fig. 3, the spectrum displays characteristic proton resonances: the ortho-phenyl protons (denoted "a") of 2-amino-MIM at δ = 6.96 ppm, the methyl protons (denoted "b") of 2-methylimidazole (a synthetic precursor to ZIF-67-NH_2 gel) at δ = 2.36 ppm, and the imidazole ring protons (denoted "c") at δ = 7.08 ppm. These chemical shifts show close agreement with literature values for 2-amino-MIM coordinated in ZIF-series MOFs[32], confirming that 2-amino-MIM is incorporated into the ZIF-67-NH_2 framework via coordination bonds, rather than through physisorption. Furthermore, integration of the peak at δ = 6.96 ppm indicates a 2-amino-MIM loading of 10.9 mol% (for calculation details, see Supplementary Note

1), which is consistent with our theoretical estimate of 10 mol%.

To explore the impact of amino modification on porosity, N_2 adsorption–desorption isotherms were collected for both ZIF-67 gel and ZIF-67-NH_2 gel (Supplementary Fig. 4 and Supplementary Table 1). The isotherms (Supplementary Fig. 4a) indicate that both materials exhibit combined microporous–mesoporous features, with pronounced hysteresis at high relative pressures ($P/P_0 \approx 1$). Compared to pristine ZIF-67 gel, ZIF-67-NH_2 gel shows a reduced N_2 uptake, suggesting a decrease in pore volume due to amino group incorporation. This reduction likely reflects subtle pore structure tuning[32]. Pore size distribution analysis (Supplementary Fig. 4b) reveals a shift in the dominant pore size from 0.77 nm (ZIF-67 gel) to 0.69 nm (ZIF-67-NH_2 gel), which may result from the steric hindrance or altered coordination environment introduced by amino groups. Specific surface area measurements further support this observation. ZIF-67-NH_2 gel exhibits a BET surface area of 1122 $m^2\ g^{-1}$, lower than the 1330 $m^2\ g^{-1}$of unmodified ZIF-67. While micropore volumes changed slightly (0.46 $cm^3\ g^{-1}$ vs. 0.50 $cm^3\ g^{-1}$), the mesopore volume decreases from 1.07 $cm^3\ g^{-1}$ to 0.88 $cm^3\ g^{-1}$, indicating that functionalization primarily reduces mesoporosity. Such pore structure refinement may be beneficial for gas separation by enhancing selectivity for smaller gas molecules (e.g., CH_4, N_2)[37]. Three independent batches of ZIF-67-NH_2 gels synthesized under identical protocols underwent duplicate BET measurements, confirming reproducible pore structures with consistent micropore sizes (0.67–0.69 nm, Supplementary Fig. 5).

To elucidate the impact of amino functionalization on ultramicroporosity, we performed CO_2 adsorption–desorption measurements. The resulting isotherms (Fig. 1i) and corresponding ultramicropore size distributions for both pristine and amino functionalized gels (Fig. 1j) were analyzed to quantify pore-structure modifications. Relative to the ZIF-67 gel, ZIF-67-NH_2 gel exhibits significantly enhanced CO_2 uptake at $P/P_0 > 0.01$, indicative of strengthened acid–base interactions and hydrogen bonding between the –NH_2 groups and CO_2 molecules[38, 39]. Furthermore, pore-size distribution analysis reveals a marked increase in ultramicropore volume within the 3–7 Å range, thereby reinforcing kinetic-diameter-based molecular sieving and elevating the

membrane's selective separation performance.

Thermogravimetric analysis (TGA) was performed to evaluate the thermal stability of the functionalized gel, as presented in Supplementary Fig. 6. A pronounced weight loss between 100–150 °C is observed for ZIF-67-NH_2 gel, while the unmodified ZIF-67 gel remains stable in this temperature range. This behavior is likely due to the increased hydrophilicity of –NH_2 groups, which promotes the adsorption of water and solvent molecules that subsequently evaporate upon heating. At elevated temperatures (400–500 °C), both gels undergo sharp weight loss, corresponding to the decomposition of the ZIF framework. The final residue is slightly lower for ZIF-67-NH_2 gel (31.79 wt%) compared to ZIF-67 gel (33.47 wt%), possibly due to the thermal degradation of the amino groups.

Characterization of ZIF-67-NH_2 Gel/6FDA-TMPD MMMs

We then synthesized the fluorinated polyimide, 6FDA-TMPD, through the step-growth polymerization of equimolar 4,4′-(hexafluoroisopropylidene) diphthalic anhydride (6FDA) and 2,3,5,6-tetramethyl-1,4-phenylenediamine (TMPD), as detailed in the experimental section. The ZIF-67 and ZIF-67-NH_2 gels were then incorporated into 6FDA-TMPD polymer matrix to fabricate MMMs with varying loadings via solution casting and solvent evaporation method. The cast membranes were first dried in a forced-air oven at 120 °C to evaporate the solvent, then further treated in a vacuum oven at 150 °C to remove residual reagents and enhance membrane integrity. To further investigate the dispersion of the MOF gels within the membrane, cryo-ultramicrotomy was employed to prepare ultrathin cross-sectional samples (60–90 nm) of the MMMs with 31 wt% ZIF-67 gel and 38 wt% ZIF-67-NH_2 gel. TEM was then used to examine their cross-sectional morphologies.

TEM images (Fig. 2a, b, left) show that both ZIF-67 and ZIF-67-NH_2 gels are uniformly distributed within the 6FDA-TMPD matrix, forming continuous MOF channels that facilitate efficient gas transport[40, 41]. Furthermore, the high-magnification TEM images (Supplementary Fig. 7 and 8) reveal that while the ZIF-67 gel forms more aggregated distributions within the matrix, the ZIF-67-NH_2 gel exhibits notably improved dispersion uniformity, with a much tighter

interfacial contact with the polymer. The differences in interfacial compatibility are also depicted in the schematics (Fig. 2a, b, right) and are further analyzed in subsequent sections. ZIF-67 gel may form non-selective voids due to poor compatibility with the polymer. Whereas, the ZIF-67-NH_2 gel integrates seamlessly into the matrix, minimizing interfacial defects, so that the gas molecules mainly transport through the MOF channels. The introduction of -NH_2 groups effectively enhances the interfacial interaction with the polymer. This improvement not only minimizes interfacial defects but also promotes uniform dispersion of the MOF gel, thereby reinforcing both the structural integrity and the gas separation performance of the membrane.

To elucidate the interaction mechanism between the ZIF-67-NH_2 gel and the 6FDA-TMPD matrix, FT-IR spectroscopy was employed. Changes in the FT-IR spectra before and after ZIF-67-NH_2 gel incorporation were analyzed to probe the nature of the intermolecular interactions. Fig. 2c illustrates the proposed interaction mechanism, including hydrogen bonding and amide bond formation. Fig. 2d-f correspond to the spectral changes associated with the key functional groups indicated in Fig. 2c. In Fig. 2d,e the pristine 6FDA-TMPD membrane shows characteristic imide absorptions at 1720 cm^{-1} (C=O stretching) and 1354 cm^{-1} (C–N stretching). With increasing ZIF-67-NH_2 content, these bands gradually weaken, while new peaks at 1654 cm^{-1} and 1577 cm^{-1} appear, corresponding to the amide I (C=O stretching) and amide II (N–H bending/C–N stretching) modes. These changes indicate that a fraction of the imide carbonyls in the polyimide rings have reacted with the amino groups of ZIF-67-NH_2 to form covalent amide (–CONH–) linkages. To further confirm the formation of new amide bonds, we conducted ^{13}C NMR spectroscopy (Supplementary Fig. 9). The ^{13}C NMR spectrum shows a distinct amide carbonyl peak at 167.3 ppm, consistent with literature reports[42]. Meanwhile, in Fig. 3f, the characteristic bands of CF_2 and CF_3 groups (1330–1030 cm^{-1}) exhibit a blue shift, implying enhanced hydrogen bonding between the fluorine atoms of the 6FDA-TMPD backbone and the N–H groups of amide structures. These synergistic covalent and hydrogen-bonding interactions effectively strengthen the interfacial adhesion, improve compatibility, and enhance the overall stability of the hybrid membranes[25, 36, 43, 44, 45, 46].

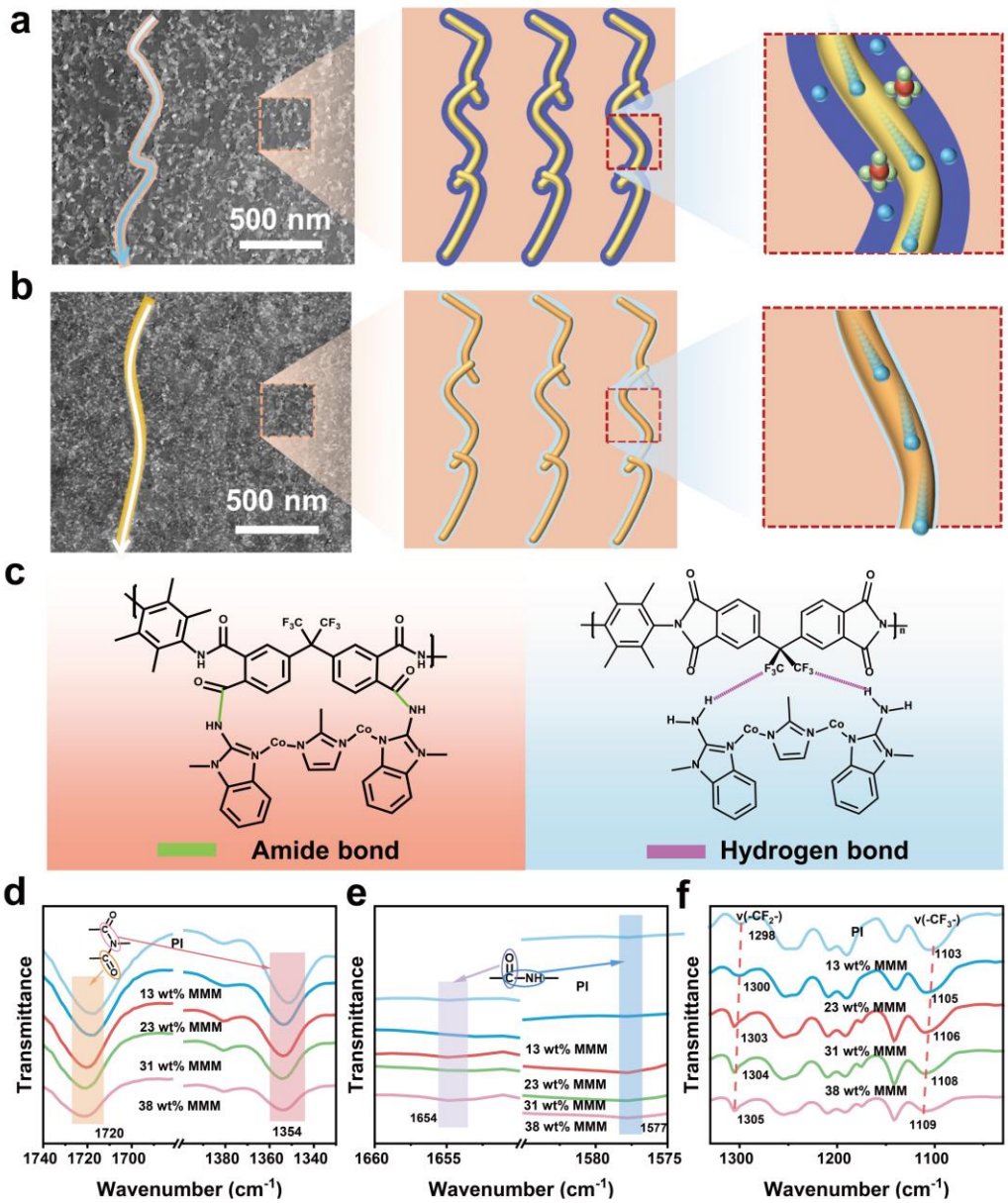

Fig. 2 Microstructure and interfacial interactions in MMMs. a) TEM image of ZIF-67 gel dispersed in the 6FDA-TMPD matrix, showing a network of interconnected MOF strands (left). The schematic illustration (right) highlights the spatial distribution of ZIF-67 gel in the polymer matrix, with a representation of nonselective gas transport channels formed within the membrane. **b)** TEM image of ZIF-67-NH_2 gel dispersed in the 6FDA-TMPD matrix, showing a similar network structure (left). The schematic illustration (right) depicts the defect-free gas transport channels formed by the ZIF-67-NH_2 gel, emphasizing enhanced selectivity. **c)** Schematic illustration of supramolecular interactions within ZIF-67-NH_2 gel/6FDA-TMPD MMMs. **d–f)** ATR-FTIR

spectra of ZIF-67-NH_2 gel/6FDA-TMPD MMMs with different loadings in selected spectral regions: **d)** 1740–1680 cm^{-1}, 1400-1330 cm^{-1}, **e)** 1660–1650 cm^{-1}, 1585–1575 cm^{-1} and **f)** 1330–1030 cm^{-1}.

To verify covalent crosslinking between amino-functionalized ZIF-67 gel and 6FDA-TMPD matrix, we assessed chemical stability of three variants—pure 6FDA-TMPD, 31 wt% ZIF-67 gel/6FDA-TMPD, and 38 wt% ZIF-67-NH_2 gel/6FDA-TMPD MMMs—after 200 days in DMF (Supplementary Fig. 10). The pure membrane dissolved fully (Supplementary Fig. 10a), while the unmodified MMMs deformed and partially disintegrated due to weak hydrogen-bonded interfaces (Supplementary Fig. 10b). The crosslinked MMMs retained sheet-like integrity with minor surface fragmentation (Supplementary Fig. 10c), stemming from rigid interfacial networks that restrict chain mobility yet block solvent swelling. For long-term stability, undeformed but slightly brittle membranes may outperform deformed ones via enhanced solvent resistance. To clarify, SEM analysis post-immersion and drying (150 °C, 12 h) shows widespread defects in 31 wt% ZIF-67 gel/6FDA-TMPD MMMs (Supplementary Fig. 11) versus smooth surfaces in 38 wt% ZIF-67-NH_2 gel/6FDA-TMPD MMMs (Supplementary Fig. 12).

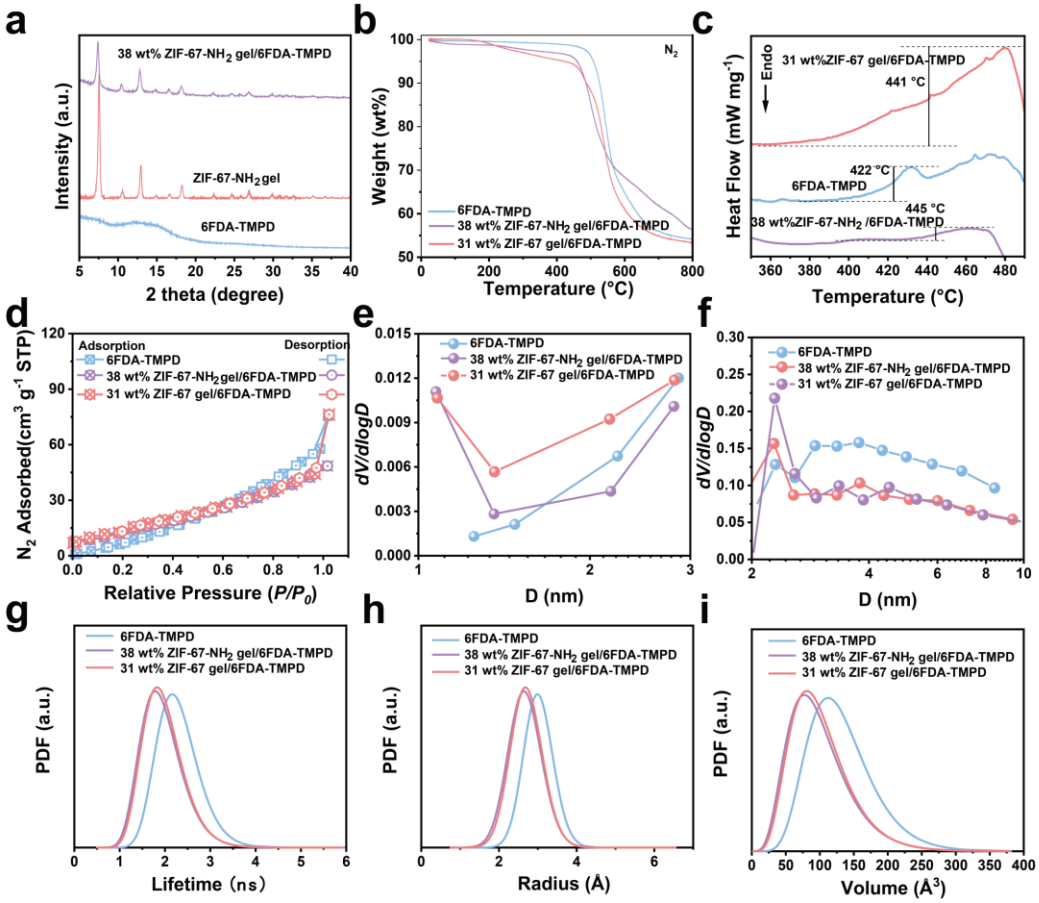

Fig. 3 Structural, thermal, and porosity analysis of MMMs. a) XRD, **b)** Thermal stability, and **c)** DSC graphs of ZIF-67-NH_2 gel/6FDA-TMPD MMMs, ZIF-67 gel/6FDA-TMPD MMMs and 6FDA-TMPD. **d)** Nitrogen adsorption-desorption isotherms (77 K), **e)** Micropore size distribution (Horvath–Kawazoe, HK method), and **f)** Mesopore size distribution (Barrett–Joyner–Halenda, BJH method) of ZIF-67-NH_2 gel/6FDA-TMPD MMMs, ZIF-67 gel/6FDA-TMPD MMMs and 6FDA-TMPD. PALS of ZIF-67-NH_2 gel/6FDA-TMPD MMMs, ZIF-67 gel/6FDA-TMPD MMMs and 6FDA-TMPD: **g)** Lifetime distribution, **h)** Radius distribution, **i)** Pore volume distribution.

To comprehensively evaluate the structural and thermal stability enhancements imparted by ZIF-67-NH_2 gel, XRD, TGA, dynamic mechanical analysis (DMA) and differential scanning calorimetry (DSC). were conducted. As shown in the XRD patterns (Fig. 3a), the MMMs display characteristic diffraction peaks corresponding to ZIF-67-NH_2 gel, confirming the retention of its crystalline structure in the polymer matrix. TGA profiles (Fig. 3b) reveal that all membranes undergo single-step decomposition. Pristine 6FDA-TMPD exhibits excellent thermal stability,

with degradation onset above 500 °C. Incorporation of 31 wt% ZIF-67 gel results in a slight decrease in thermal stability, likely due to poor interfacial compatibility, which introduces structural defects and facilitates early thermal degradation. In contrast, the membrane containing 38 wt% ZIF-67-NH_2 gel maintains thermal stability comparable to the neat polymer. This enhanced thermal resistance is attributed to the improved interfacial interaction between the amino-functionalized MOF gel and the polymer matrix, which suppresses defect formation and promotes more homogeneous dispersion. Polymer–filler interactions were probed using DMA and DSC. DMA measurements (Supplementary Fig. 13) revealed that the incorporation of MOF fillers increased the storage modulus of the membranes, indicating reduced polymer chain mobility[47]. Notably, the ZIF-67-NH_2 gel MMMs more effectively restricted polymer flexibility compared to their ZIF-67 gel counterparts, likely due to stronger interactions between the amino-functionalized MOF and the polymer, leading to greater confinement of the polymer chains. However, the membranes fractured before reaching their glass transition temperature (Tg) during DMA testing, preventing direct determination of the MMMs' Tg. The Tg of all samples was further characterized via DSC analysis (Fig. 3c). The Tg of pure 6FDA-TMPD is 422 °C, which is in agreement with previously reported values for 6FDA-TMPD[48]. The incorporation of ZIF-67 gel and ZIF-67-NH_2 gel leads to an increase in Tg, with larger increments observed in the ZIF-67-NH_2 gel MMMs (Tg 445 °C). Together, these results confirm that the ZIF-67-NH_2 gel samples exhibit more pronounced restrictions on polymer chain mobility, due to enhanced interfacial adhesion and improved compatibility[49].

To further examine the effects of ZIF-67-NH_2 gel on the pore characteristics of membrane, nitrogen adsorption–desorption measurements were conducted to evaluate the influence of MOF gel incorporation on membrane porosity with the results shown in Fig. 3d-f and summarized in Supplementary Table 2. The pristine 6FDA-TMPD membrane exhibits a low BET surface area (23 $m^2\ g^{-1}$), with dominant mesoporosity (0.149 $cm^3\ g^{-1}$) and minimal microporosity (0.003 $cm^3\ g^{-1}$). Incorporation of 31 wt% ZIF-67 gel increases the surface area to 54 $m^2\ g^{-1}$ and total pore volume to 0.141 $cm^3\ g^{-1}$, primarily due to an increase in mesopore volume. This broadening of

mesoporosity likely arises from poor interfacial compatibility, resulting in interparticle voids or structural defects. By contrast, the MMM containing 38 wt% ZIF-67-NH_2 gel shows a moderate BET surface area (44 $m^2 g^{-1}$), but a significantly enhanced micropore volume (0.013 $cm^3 g^{-1}$) and reduced mesoporosity (0.089 $cm^3 g^{-1}$), indicating a more compact and defect-free structure. The average pore size (0.68 nm) is comparable to that of the ZIF-67 gel MMMs but reflects a more uniform microporous network. The improved microporosity and reduced mesopore contribution in ZIF-67-NH_2 gel-based membranes are expected to favor selective gas transport and structural stability.

The reproducibility of the 38 wt% ZIF-67-NH_2 gel/6FDA-TMPD MMMs was validated by three independent syntheses under controlled conditions. To resolve the microporous architecture, CO_2 adsorption (273 K) analyzed via the non-local density functional theory (NLDFT) model was employed. As shown in **Supplementary Fig. 14**, the resulting pore size distributions exhibit high consistency across batches, confirming the excellent reproducibility of the MMMs' microporous network.

Since BET analysis cannot sufficiently resolve the pore size distribution in the ultramicroporous regions of MMMs, positron annihilation lifetime spectroscopy (PALS) was employed to further investigate the effects of incorporating ZIF-67 gel and ZIF-67-NH_2 gel on the free-volume architecture and ultramicroporosity of 6FDA-TMPD membranes. The resulting positron-lifetime spectrum (Fig. 3h), pore-radius distribution (Fig. 3i), and pore-volume distribution (Fig. 3g) provide a comprehensive dataset—summarized in Supplementary Table 3—enabling an in-depth evaluation of structural evolution. The pristine 6FDA-TMPD membrane exhibits a lifetime of 2.29 ns, reflecting a relatively larger free-volume and a more extended microporous structure. The pore radius is 3.10 Å, with a pore volume of 125.5 $Å^3$, corresponding to a fractional free volume (FFV) of 11.99% (calculated based on the spherical potential well model, see Supplementary Note 2 for details.) Incorporation of 38 wt% ZIF-67-NH_2 gel results in a significant reduction in lifetime to 1.94 ns, indicating a more compact free-volume structure. The pore radius decreases to 2.79 Å, and the pore volume reduces to 91.36 $Å^3$, yielding a FFV of 9.91%.

These changes suggest that the amino-functionalized ZIF-67 gel enhances the interfacial compatibility with the polymer matrix, leading to a denser, more compact membrane structure with reduced free volume, potentially improving selective gas transport performance. In contrast to the 38 wt% ZIF-67-NH_2 gel/6FDA-TMPD MMMs, the incorporation of 31 wt% ZIF-67 gel into the MMMs results in a lifetime of 1.97 ns, a pore radius of 2.82 Å, and a pore volume of 94.1 $Å^3$, corresponding to a FFV of 8.47%. This moderate reduction in free volume is linked to the relatively weaker interaction between ZIF-67 gel and the 6FDA-TMPD matrix. The diminished interfacial bonding leads to the formation of more structural defects, which consequently causes a slight increase in both pore radius and pore volume. Additionally, the observed decrease in FFV can be attributed to the lower loading of ZIF-67 gel within the MMMs, which may restrict the development of additional free volume in the ultramicroporous regions. PALS analysis indicates that the incorporation of ZIF-67-NH_2 gel facilitates the formation of a denser and more structurally coherent pore architecture, reflecting improved interfacial compatibility between ZIF-67-NH_2 gel and the 6FDA-TMPD matrix. This improved structural integration, particularly within the ultramicroporous regime, is anticipated to significantly enhance the He/CH_4 selectivity of the membrane.

To confirm the actual loading of fillers within the MMMs, TGA analysis was performed on membranes containing 38 wt% ZIF-67-NH_2 gel (Supplementary Fig. 15). Based on mass conservation principles, the final residue of the MMMs should correspond to the weighted average of the residues of the polymer and filler. In this study, the pure polymer and ZIF-67-NH_2 gel exhibited residues of 5.85 wt% and 31.79 wt%, respectively, while the MMM showed a residue of 15.67 wt%. The calculated filler loading was 37.78 wt%, in excellent agreement with the theoretical value of 38 wt%, confirming the reliability of the fabrication process and the accuracy of the TGA-based quantification.

The mechanical properties of the ZIF-67 gel and ZIF-67-NH_2 gel MMMs, along with the pristine 6FDA-TMPD membrane, were measured and are summarized in Supplementary Fig. 16. The ZIF-67-NH_2 gel MMMs at 13 and 23 wt% loadings demonstrate higher tensile strengths (50

and 47 MPa) than the pristine 6FDA-TMPD membrane (45 MPa). At equivalent loadings, the ZIF-67-NH_2 gel MMMs also show superior mechanical strength compared to the ZIF-67 gel MMMs. This indicates that the amide bonds at the interface enhance the mechanical properties of the MMMs.

Gas Separation Performance

To evaluate the effect of amino functionalization on the gas separation performance of MMMs, single-gas permeation experiments were conducted for He and CH_4 using the constant pressure–variable volume method at 1 bar and 35 °C. MMMs containing varying loadings of ZIF-67-NH_2 gel and ZIF-67 gel in a 6FDA-TMPD matrix were tested, and the results are presented in Fig. 4a, b.

As the ZIF-67-NH_2 gel loading increased, the He permeability initially decreased and subsequently increased sharply, while the He/CH_4 selectivity continuously improved. The initial reduction in permeability is attributed to the decrease in free volume caused by hydrogen bonding and covalent crosslinking between amino groups and the polymer matrix. At higher loadings, the formation of continuous transport pathways facilitated enhanced He permeability. Importantly, owing to the strong interfacial interactions between the ZIF-67-NH_2 gel and 6FDA-TMPD matrix, the He/CH_4 selectivity did not decline but instead increased significantly. At a 38 wt% loading, the He permeability reached 549 Barrer and the He/CH_4 selectivity increased to 110.3—representing a 10.1-fold enhancement relative to pristine 6FDA-TMPD (10.9). This performance surpasses the 2008 Robeson upper bound for He/CH_4 separation and exceeds that of most reported MMMs for this gas pair (Fig. 4c and Supplementary Table 4). To demonstrate the practical relevance of our approach, we compared the membrane with Matrimid, a widely used polyimide that typically exhibits a He permeability of 10~50 Barrer and a He/CH_4 selectivity of 100[50, 51, 52]. Our membranes show comparable selectivity but a 10- to 50- fold higher He permeability, implying a substantially reduced membrane are requirement. Given the practical benefits of lower membrane area, we further compared with other high-permeability membranes (P_{He} > 50 Barrer). As summarized in Supplementary Fig. 17 and Supplementary Table 5, the permeability and

selectivity enhancement ratios of representative systems highlight that our strategy achieves a more pronounced improvement in selectivity, whereas most reported systems exhibit less than a twofold enhancement.

We further assessed how higher amino content in ZIF-67-NH_2 gels influences MMM performance. As shown in Supplementary Table 4, MMMs fabricated using ZIF-67-NH_2 gels with 14.5 mol% (Supplementary Fig. 18) and 22.7 mol% (Supplementary Fig. 19) 2-aminobenzimidazole exhibited improved He/CH_4 selectivity (rising from 110.3 to 158.1) alongside a modest reduction in He permeability (declining from 549.0 to 479.7 Barrer). This trade-off stems from the narrower micropores of high-amino-content gels (0.64 nm versus 0.69 nm, as shown in Supplementary Fig. 20 and Supplementary Table 1), which increase mass transfer resistance and enhance size-sieving ability of the MMMs.

To assess the broad applicability of the ZIF-67-NH_2 gel, we further evaluated two other polymers (6FDA-PMDA-FDA-53 and Matrimid, detailed information provided in Supplementary Note 3 and Note 4). For 6FDA-PMDA-FDA-53, the neat polymer has a He permeability of 125.8 Barrer and He/CH_4 selectivity of 16.4. The 38 wt% ZIF-67-NH_2 gel/6FDA-PMDA-FDA-53 MMMs shows a He permeability of 100.2 Barrer and He/CH_4 selectivity of 85.6, a 5.2-fold gain. For Matrimid, the neat polymer exhibits a He permeability of 35.9 Barrer and He/CH_4 selectivity of 113.8. The 38 wt% ZIF-67-NH_2 gel/Matrimid MMMs gives a He permeability of 31.5 Barrer and He/CH_4 selectivity of 256.7, a 2.3-fold gain. These results are now in Supplementary Table 4.

We further synthesized MMMs with higher filler contents (43 wt%, 47 wt%, and 51 wt%). As shown in Supplementary Fig. 21, these higher-loading membranes fractured into small, fragmented pieces and failed to form intact, self-supporting sheets, rendering them unsuitable for gas permeation testing. This structural failure is attributed to the increased internal stress within the membrane, as the rigid MOF gel domains restrict polymer chain mobility and compromise mechanical integrity.

These results demonstrate that the incorporation of ZIF-67-NH_2 gel effectively optimizes the pore structure of the MMMs through hydrogen bonding and crosslinking interactions, thereby

enhancing gas separation selectivity while maintaining high permeability. In contrast, ZIF-67 gel/6FDA-TMPD MMMs (Fig. 4b), lacking amino functionalization, exhibited weaker interfacial compatibility with the polymer matrix. Consequently, He permeability increased gradually with filler loading, reaching a maximum of 1404 Barrer at 31 wt%. However, the He/CH_4 selectivity remained low at only 12.6. Moreover, at a filler loading of 38 wt%, the membrane failed to form an integral structure due to poor interfacial adhesion and uneven stress distribution, rendering gas permeation testing infeasible. Overall, the amino functionalization of ZIF-67 gel not only improves compatibility with the polymer matrix but also enhances pore structure and gas selectivity, resulting in outstanding performance for He/CH_4 separation. In contrast, non-functionalized ZIF-67 gel struggles to maintain efficient separation at high loading levels.

To comprehensively evaluate the membrane performance and underlying transport mechanism, we determined the gas permeability (P), diffusion (D) and solubility (S) coefficients of He and CH_4 at 35 °C using the time-lag method (Fig. 4d–f). Incorporation of 38 wt% ZIF-67-NH_2 gel into the 6FDA-TMPD matrix decreased both D(He) and D(CH_4) relative to the neat polymer; however, the diffusion selectivity D(He)/D(CH_4) and solubility selectivity S(He)/S(CH_4) increased by factors of 3.95 and 2.68, respectively. This enhancement is attributed to hydrogen- and covalent-bonding between ZIF-67-NH_2 and 6FDA-TMPD, which contracts mesopores while expanding micropores. The resulting defect-free, continuous transport channels preserve He mobility (D(He) only drops by 38%), whereas CH_4 diffusion is severely hindered (D(CH_4) decreases by 84%), thereby enabling precise He/CH_4 separation. By contrast, 31 wt% ZIF-67 gel/6FDA-TMPD MMMs exhibit a modest increase in D(He) but also abundant nonselective interfacial voids that boost CH_4 solubility and flux, mitigating any net gain in He/CH_4 selectivity.

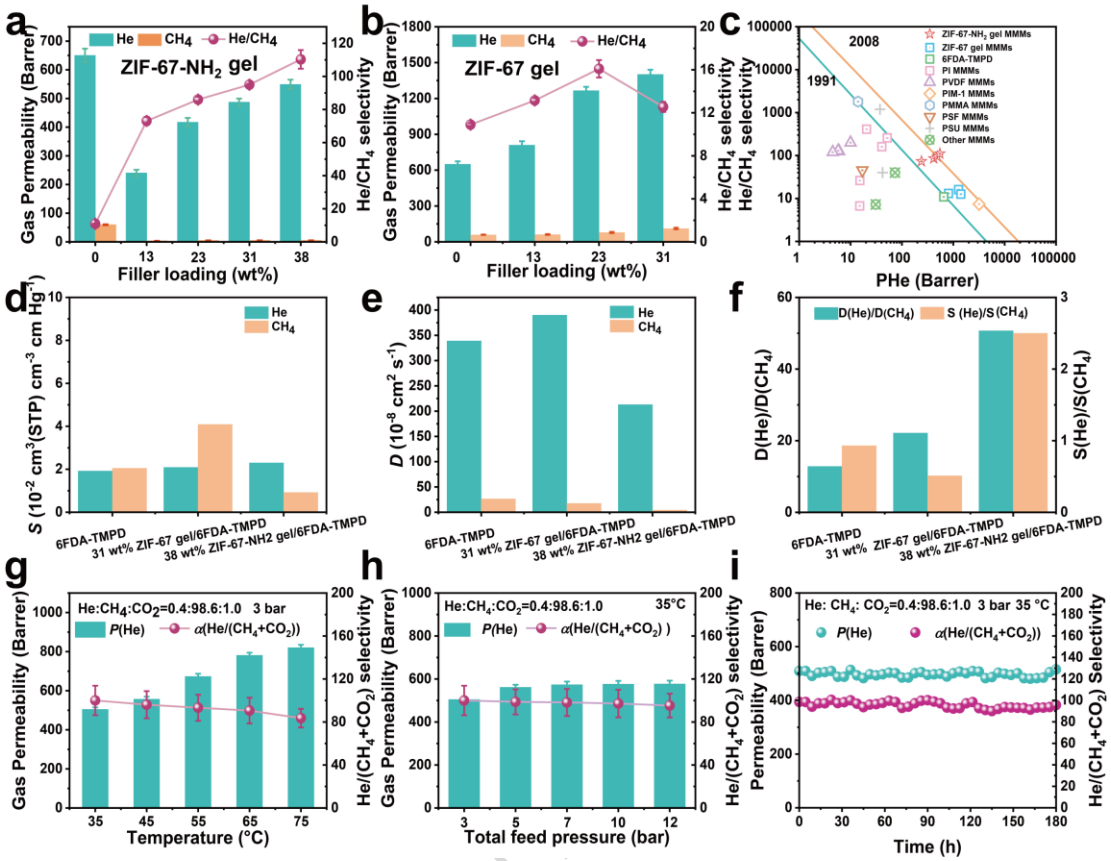

Fig. 4 Separation efficiency and stability of MMMs. a) Enhancement of He permeability and He/CH_4 selectivity of ZIF-67-NH_2 gel/6FDA-TMPD MMMs with different loadings, **b)** Enhancement of He permeability and He/CH_4 selectivity of ZIF-67 gel/6FDA-TMPD MMMs with different loadings, **c)** Comparison of He/CH_4 separation performance of ZIF-67-NH_2 gel/6FDA-TMPD MMMs with other reported MMMs in the literature (Source data are provided in Supplementary Table 4.). **d)** Diffusion coefficients and **e)** solubility coefficients of ZIF-67-NH_2 gel/6FDA-TMPD MMMs, ZIF-67 gel/6FDA-TMPD MMMs and 6FDA-TMPD. **f)** He/CH_4 diffusion and solubility selectivity of 38 wt% ZIF-67-NH_2 gel/6FDA-TMPD MMMs, 31 wt%ZIF-67 gel/6FDA-TMPD MMMs and 6FDA-TMPD. Mixed gas separation performance of 38 wt% ZIF-67-NH_2 gel/6FDA-TMPD MMMs under industrial conditions: **g)** He/(CH_4+CO_2) separation performance at different temperatures; **h)** He/(CH_4+CO_2) separation performance at different operating pressures (3–12 bar) and 35 °C; **i)** Long-term separation stability at a feed ratio of He/(CH_4+CO_2) = 0.4:98.6:1.0, feed pressure of 3 bar, and temperature of 35 °C. Error bars represent the standard deviation (SD) derived from n = 3 independently fabricated membrane samples.

To assess the industrial relevance of the 38 wt% ZIF-67-NH_2 gel/6FDA-TMPD mixed-matrix membrane, we conducted mixed-gas separations under representative process conditions (He:CH_4:CO_2=0.4:98.6:1.0 vol%). We systematically evaluated the influence of temperature,

pressure and extended operation on performance (Fig. 4g-i). With rising temperature (Fig. 4g), He permeability increased markedly, whereas He/(CH_4+CO_2) selectivity diminished gradually. This behavior reflects enhanced segmental mobility at elevated temperatures, which enlarges interchain free volume, attenuates size-sieving and thus reduces discrimination against larger CH_4 and CO_2 molecules. Under feed pressures ranging from 3 to 12 bar (Fig. 4h), He permeability exhibited a modest pressure dependence, while selectivity remained essentially invariant, evidencing robust separation performance across industrially relevant pressures. Long-term stability tests at 35 °C and 3 bar over 180 h (Fig. 4i) demonstrated that the membrane preserves more than 95% of its initial separation performance, attesting to its remarkable operational robustness. These results underscore that amino-functionalized ZIF-67 gel not only enhances gas-transport efficiency but also confers sustained mechanical integrity and thermal resilience, affirming its suitability for industrial-scale gas-separation processes.

3.3 Techno-economic analysis

To assess the separation performance and economic viability of 38 wt% ZIF-67-NH_2 gel/6FDA-TMPD mixed matrix membranes (MMMs) under practical conditions—and to enable a direct performance comparison with commercial alternatives—a well-mixed flow model was implemented in MATLAB R2024b (code in the Supporting Information). This model assumes uniform gas concentrations on both the feed (retentate) and permeate sides of the membrane module. The analysis considered the 38 wt% ZIF-67-NH_2 gel/6FDA-TMPD MMMs, which exhibited a He permeance of 576 GPU (assuming the membrane thickness of 1 μm) and a He/CH_4 selectivity of 95 under mixed-gas conditions, alongside commercial membranes such as polysulfone (PSF) and polyimide (PI), with performance data for neat PI and PSF sourced from the literature[53].

Cost calculations encompassed fixed investment (membrane price: 78.8 \$ m^{-2}; heat exchanger cost 5% of fixed investment[54], assumed proportional to feed flow rate), maintenance, and energy consumption, with compressor/expander efficiency set at 85%. Additionally, key computational formulas critical for these calculations are systematically listed in Supplementary Table 6. Single-

stage membrane separation simulations were conducted under identical conditions: 30 bar feed pressure, 1 bar permeate pressure, 0.4:99.6 mol% He/CH_4 feed, 100 $m^3 s^{-1}$ (70.74 kg s^{-1}) feed flow rate, 1.0 mol% He purity in permeate, and 6000 h annual operation. The resulting data from these simulations, which directly inform the economic and performance evaluations, are succinctly presented in Fig. 5a and Supplementary Table 7. The well-mixed model revealed that single-stage separation efficiency is primarily governed by the pressure ratio rather than membrane selectivity, as mass transfer is driven by the partial pressure differential between the feed and permeate. However, higher pressure ratios are often limited in practice by equipment constraints and energy costs. Highly selective membranes (e.g., neat PI) require larger membrane areas due to low permeance, raising costs. Indeed, neat PI and PSF membranes, both with selectivities exceeding 150, were found to require prohibitively large surface areas. By contrast, the 38 wt% ZIF-67-NH_2 gel/6FDA-TMPD MMMs achieved the desired separation performance with a membrane area of only 279 m^2—a reduction of 89.6% to 98.8% compared to neat membranes.

To further clarify this performance and address the inherent trade-off between permeance and selectivity, we extended our techno-economic analysis to include representative literature examples that lie at the extremes of the performance spectrum (Supplementary Table 7). Specifically, we compared our MMMs with a high-selectivity/low-permeance NH_2-UiO-66/PMMA MMM and a high-permeance/low-selectivity ZIF-8/PIM-1 MMM, assuming the membrane thickness of 1 μm. Under identical simulation conditions, the NH_2-UiO-66/PMMA membrane, despite its exceptional He/CH_4 selectivity (~1800), required an impractical membrane area exceeding 220,000 m^2 due to its very low permeance (14 GPU), resulting in the highest total cost. Conversely, the ZIF-8/PIM-1 membrane, while offering very high permeance (3180 GPU), suffered from low He recovery (70.33%) and higher energy consumption due to its low selectivity (7.4), leading to a higher total cost than our MMM despite its smaller area requirement. These findings underscore that the most economically desirable membrane is not one that maximizes either permeance or selectivity in isolation, but rather one that optimally balances these two properties. Our 38 wt% ZIF-67-NH_2 gel/6FDA-TMPD MMMs, by virtue of this balanced

performance, achieves a compact design, high recovery, low energy consumption, and the lowest total cost among the compared systems.

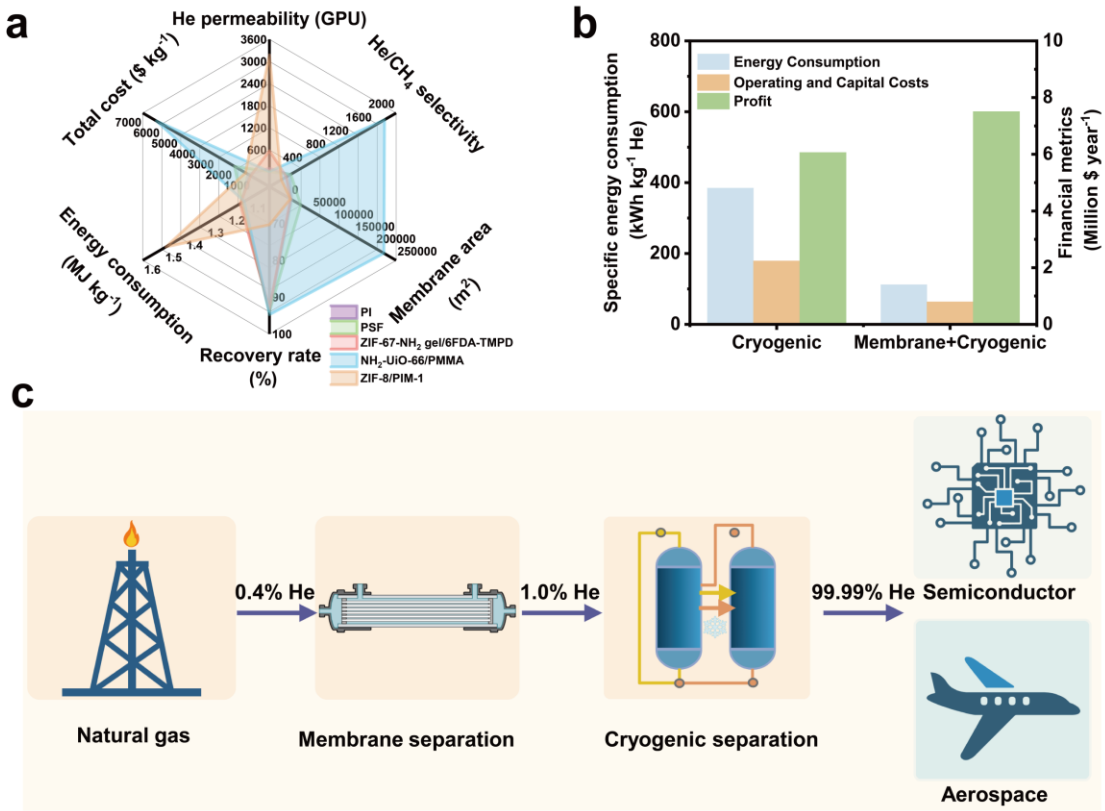

Fig. 5. Techno-economic evaluation of helium recovery. a) Radar plot comparing performance metrics of single-stage membrane separation using various materials: He permeance, He/CH_4 selectivity, membrane area, recovery rate, energy consumption, and total cost (Source data are provided in Supplementary Table 7.). **b)** Aspen Plus® V11-based comparison of cryogenic versus membrane–cryogenic hybrid in terms of energy consumption, cost, and annual profit. **c)** Schematic of helium enrichment from natural gas via membrane separation followed by cryogenic, achieving 99.99% purity for semiconductor and aerospace applications.Created in BioRender. Keming, Z. (2026) https://BioRender.com/51u3o3b.

To further assess the industrial applicability of the 38 wt% ZIF-67-NH_2 gel/6FDA-TMPD MMMs, the membranes were incorporated into Aspen Plus® V11 for process-scale simulation and full techno-economic evaluation with results depicted in Fig. 5b. Detailed process flow diagrams for the standalone cryogenic and membrane-integrated systems are provided in Supplementary Figs. 22 and 23, respectively, while a schematic representation of the membrane-cryogenic hybrid

system is provided in Fig. 5c. Both configurations were designed to enrich helium from an initial concentration of 0.4 mol% to electronic-grade purity (>99.999999 mol%), meeting stringent industrial requirements. In the baseline cryogenic system, helium recovery required 412.7 kWh kg^{-1} He and high capital investment. By introducing the 38 wt% ZIF-67-NH_2 gel/6FDA-TMPD MMMs as a pre-separation unit, the specific energy consumption was reduced by ~73%, while the cryogenic unit size and capital cost were cut by approximately half. Although helium sales revenue slightly declined, the overall annual profit increased to $8.10 M, representing a ~19% improvement compared to the conventional system. These findings demonstrate that the membrane–cryogenic hybrid process markedly enhances both energy efficiency and economic performance, offering a scalable and cost-effective solution for large-scale helium recovery from methane-rich streams.

In summary, we have developed a MOF-crosslinked MMM featuring an amino-functionalized ZIF-67 gel network uniformly embedded within a 6FDA-TMPD polyimide matrix, delivering outstanding He/CH_4 separation performance. The synergistic covalent and hydrogen-bonding interactions between the ZIF-67-NH_2 gel and the polymer matrix effectively eliminate interfacial voids, resulting in the formation of continuous, and size-selective MOF nanochannels. This architecture enables the membrane to attain a He permeability of 549 Barrer and a He/CH_4 selectivity of 110.3, surpassing the 2008 Robeson upper bound. Under industrially relevant mixed-gas conditions (He/CH_4/CO_2 = 0.4:98.6:1.0 vol%), the membrane demonstrates exceptional operational stability, maintaining over 95% of its initial performance after 180 hours. Aspen Plus® simulations of a hybrid membrane-cryogenic separation system for a 1,000 kmol h^{-1} feed further reveal the economic advantages of our MMM, including a 74% reduction in specific energy consumption (from 385 to 112.6 kWh kg^{-1} He), a 50% decrease in downstream capital expenditure, and a 24% increase in annual net profit (from USD 6.06 M to 7.50 M), while ensuring a helium recovery rate exceeding 93%. These results demonstrate that the tailored interfacial chemistry of MOF-gel fillers delivers significant economic and environmental advantages for helium recovery. This work establishes a robust, scalable engineering pathway—spanning material design, membrane fabrication, process integration, and economic evaluation—for energy-efficient, high-

purity helium separation, and lays the groundwork for broader implementation in other industrial gas-separation applications.

Methods

Materials:

2-Methylimidazole (>99.0%) was obtained from Shanghai Dibai Biotechnology Co., Ltd. Methanol (MeOH, AR), ethanol (EtOH, AR), and cobalt (II) nitrate hexahydrate ($Co(NO_3)_2 \cdot 6H_2O$), >99.0%) were supplied by Sinopharm Chemical Reagent Co., Ltd. (Shanghai). Triethylamine (TEA, >99.0%), 4,4'-(hexafluoroisopropylidene)diphthalic anhydride (6FDA, >99.0%), 2,3,5,6-tetramethyl-1,4-phenylenediamine (TMPD, >99.0%), pyromellitic dianhydride (PMDA, >99.0%), bis(4-aminophenyl)fluorene (FDA, >99.0%), m-cresol (>99.0%), isoquinoline (>97.0%), and 2-aminobenzimidazole (97%) were purchased from Shanghai Aladdin Biochemical Technology Co., Ltd. Gases, including CH_4, CO_2, Ar, and He (all 99.999%), were supplied by Changsha Mende Gas Co., Ltd.

Synthesis of ZIF-67-NH_2 Gel

The ZIF-67-NH_2 gel was synthesized via a coordination modulation–induced gelation strategy utilizing a mixed-ligand approach[16, 31, 32], as illustrated in Fig. 1a. Initially, 2.0 g of cobalt (II) nitrate hexahydrate ($Co(NO_3)_2 \cdot 6H_2O$), 4.04 g of 2-methylimidazole, and 0.76 g of 2-aminobenzimidazole (with a metal ion-to-ligand molar ratio of 1:8) were each dissolved in 20 mL of methanol (MeOH). The 2-methylimidazole solution was then added to the $Co(NO_3)_2 \cdot 6H_2O$ solution, followed by the addition of 0.8 mL triethylamine (TEA). The mixture was stirred at room temperature at 600 rpm for 1 h. Subsequently, the mixture was transferred to centrifuge tubes and centrifuged at 10690 g for 10 min. The supernatant was discarded, and the precipitate was washed three times with anhydrous MeOH, each followed by centrifugation under identical conditions. Unless otherwise specified, the "ZIF-67-NH_2 gel" referred to the material has amino ligand ratio of 10%. For ZIF-67-NH_2 (15) and (20) gels with higher amino group contents, their synthesis followed the same coordination modulation-induced gelation strategy but with adjusted 2-methylimidazole/2-aminobenzimidazole amounts (detailed protocols in Supplementary Note 5).

Synthesis of 6FDA-TMPD

The high-performance polyimide 6FDA-TMPD was synthesized according to the procedure reported previously[30, 55]. Specifically, 10 mmol of 4,4′-(hexafluoroisopropylidene) diphthalic anhydride (6FDA) and 10 mmol of 2,3,5,6-tetramethyl-1,4-phenylenediamine (TMPD) were accurately weighed and added to a reaction tube. m-Cresol was added to adjust the solid content to 30%. After purging with argon, the mixture was stirred at 30 °C for 30 min. The temperature was then raised to 60 °C, and three drops of isoquinoline were added. The reaction temperature subsequently increased in 30 °C increments every 30 min. Upon reaching 180 °C, the mixture was maintained at this temperature for 2 h, yielding a viscous, transparent yellow solution. This solution was poured into industrial ethanol to precipitate a white fibrous solid. The product was purified via Soxhlet extraction for 4 h and dried in a forced-air oven to obtain pure 6FDA-TMPD. The molecular weight details of the 6FDA-TMPD polymer are presented in Supplementary Fig. 24 and Supplementary Table 8.

Fabrication of ZIF-67-NH_2 Gel/6FDA-TMPD MMMs

ZIF-67-NH_2 gel/6FDA-TMPD MMMs were fabricated using a solution casting and solvent evaporation method, with ZIF-67-NH_2 loadings of 13.0 wt%, 23.0 wt%, 31.0 wt%, and 38.0 wt%. To prepare the casting solution, 0.15 g of 6FDA-TMPD was dissolved in 3 wt% N,N-dimethylformamide (DMF) and filtered through a 0.45 μm PTFE membrane. Prior to mixing with the polymer solution, the solvent in the ZIF-67- NH_2 gel was exchanged from MeOH to DMF via high-speed centrifugation to ensure uniform dispersion. The concentration of the DMF-dispersed gel was determined by thermogravimetric analysis (TGA), which guided the formulation of MMMs with varying filler loadings. The 6FDA-TMPD solution was then added to the MOF dispersion and stirred for 12 h to ensure homogeneity. The resulting solution was cast into 6.0 cm glass molds and dried at 120 °C in a forced-air oven for 12 h. The resulting membranes were immersed in MeOH for 12 h and subsequently dried in a vacuum oven at 150 °C for 24 h. A membrane area of 28.26 cm^2 was finally obtained. Each formulation was prepared in triplicate to ensure reproducibility. The thicknesses of the resulting intact MMMs are provided in

Supplementary Table 4.

Characterization of ZIF-67-NH_2 Gel/6FDA-TMPD MMMs

FT-IR were recorded on a Thermo Scientific Nicolet iS20 spectrometer over 4000–500 cm^{-1}. XRD patterns were collected on a Bruker D8 Advance diffractometer (45 kV, 200 mA) at 5° min^{-1} from 5° to 40°. Morphology and framework integrity were examined by TEM (Thermo Scientific Themis Z 3.2). The morphological structure of the membrane was investigated with a SEM (Regulus 8100, Japan). Nitrogen adsorption–desorption isotherms at 77 K and CO_2 isotherms at 273 K were measured on a JWGB JW-BK 200C analyzer after degassing all samples at 150 °C for 12 h, yielding brunauer-emmett-teller (BET) surface areas, micropore volumes and ultramicropore size distributions. TGA (Netzsch STA 449 F3) was performed from 25 to 800 °C at 10 °C min^{-1} under a nitrogen atmosphere to evaluate thermal stability, and under an air atmosphere to determine the actual filler loadings in the MMMs. To demonstrate the actual ratio of the mixed ligand in the MOF, we performed ^{1}H NMR using an Ascend 400 instrument (400MHz, Bruker, USA). The sample was prepared by degassing he MOF particles at 150 °C for 12 h and digesting the samples in $D_2(SO_4)/CD_3OD$ (v/v = 10/90) solution. Solid-state ^{13}C NMR spectra were acquired on a Bruker Avance 400 MHz spectrometer to confirm the formation of amide bonds in the MMMs. Polymer molecular weights and dispersities were determined by GPC (Agilent GPC 50; DMF mobile phase), with samples prepared at 0.1–0.5 wt% in DMF, sonicated and filtered through a 0.45 μm PTFE membrane. Positron annihilation lifetime spectroscopy (PALS, TechnoAP APV8002) provided quantitative insight into microdefect populations and free-volume hole distributions. DMA testing was performed on a NETZSCH DMA242E with oscillation temperature ramp mode. The sample size was prepared as ca. 10 mm by 15 mm. Measurements were taken at a frequency of 1 Hz and an amplitude of 10 μm in the range of 30 °C to 250 °C at a rate of 3 °C min^{-1}. The viscosity and flow behavior of suspensions were investigated using a modular compact rheometer, model number MCR 302e (Anton Paar, Graz, Austria). Mechanical properties of membranes were evaluated by an electronic tensile machine (Qinan Fengzhi WDW-05D). The glass transition temperatures of membrane samples were characterized by DSC (NETZSCH DSC 204 F1) in heat-

flux mode. For high-resolution and Objective Lens Spherical Aberration Corrected TEM of membrane cross sections, $\leqslant 1$ mm^3 specimens were high-pressure frozen, freeze-substituted, epoxy-embedded, and sectioned to 50–100 nm on a Leica EM-UC7 cryo-ultramicrotome.

Measurements of Gas Permeation

The gas permeation performance of the membranes was evaluated at 35 °C using the constant pressure–variable volume method. The equipment as described in a previous study[16, 34, 56] was utilized to assess both pure and mixed gas permeation capabilities of the flat-sheet membranes (Supplementary Fig. 25). The flow rate of sweep gas (Ar) was fixed at 5 mL min^{-1} using a mass flow meter. A circular membrane disc with an effective permeation area of 12.5 cm^2 was used. A FULI 9790 gas chromatograph equipped with a flame ionization detector (FID) and a thermal conductivity detector (TCD) was used to analyze the He and CH_4 concentrations in the feed and permeate gases. The permeability (P_i, Barrer; 1 Barrer = 1×10^{-10} cm^3 (STP) cm (cm^2 s cmHg)$^{-1}$) of both gases was measured after reaching a steady state, with each set of data obtained from at least three replicates. The gas permeability was calculated using Equation (1):

$$P_i = \frac{Q_i l}{\Delta p_i A} \quad \textbf{(1)}$$

where Q_i represents the volumetric flow rate of gas 'i' (cm^3 s^{-1} (SPT)), l is the membrane thickness (μm), A is the effective membrane area and Δp_i is the trans-membrane pressure difference (cmHg).

The ideal selectivity of gas 'i' and 'j' was computed using Equation (2):

$$\alpha_{i/j} = P_i / P_j \quad \textbf{(2)}$$

Gas diffusion and solution were measured at 35 °C under a feed pressure of 1 bar using pure He and CH_4 gases, utilizing a home-made constant volume/variable pressure instrument with a time-lag apparatus, starting with an oil-free high vacuum.

The apparent diffusion coefficient D (cm^2 s^{-1}) for the gas in the polymer film was calculated using Equation (3):

$$D = \frac{l^2}{6\theta} \quad \textbf{(3)}$$

where θ is the time-lag in the permeability measurement.

The solution of the gas in the polymer matrix was determined indirectly using Equation (4):

$$S = \frac{P}{D} \quad \textbf{(4)}$$

The diffusion selectivity and solubility selectivity for pure gas '*i*' and '*j*' are defined as Equation (5) and (6):

$$\alpha_{D(i/j)} = \frac{D_i}{D_j} \quad \textbf{(5)}$$

$$\alpha_{S(i/j)} = \frac{S_i}{S_j} \quad \textbf{(6)}$$

Techno-economic evaluation

Economic evaluation was carried out in two stages. First, under a fixed feed composition (He: CH_4=0.4:99.6 mol%), MATLAB R2024b was used to implement steady-state mass-balance and well-mixed flow model to concentrate helium to 1.0 mol% over the same processing conditions for both our 38 wt% ZIF-67-NH_2/6FDA-TMPD MMMs and conventional commercial membranes. Key performance metrics—including specific energy consumption, required membrane area, capital and operating costs, and He recovery—were computed for each membrane, and the composite membrane, which demonstrated the most favorable trade-off among these metrics, was selected for the next stage. In the second stage, the selected membrane was integrated into an Aspen Plus® V11 flowsheet coupled with a Cryogenic unit, and compared against a standalone Cryogenic process. Simulated compression, refrigeration and cryogenic duties were used to calculate total energy consumption and operating expenses (assuming \$0.05 kWh^{-1} electricity), while equipment and membrane capital costs were estimated via vendor correlations and annualized over their respective lifetimes (25 years for cryogenics, five years for membranes). Helium sales revenue (assumed \$100 kg^{-1}) and continuous operation at 6 000 h $year^{-1}$ enabled

estimation of net profit for both the hybrid membrane–cryogenic and the pure cryogenic routes. Continuous ±20% sensitivity analyses on electricity price and membrane cost further assessed economic robustness.

Generative AI in scientific writing

During the preparation of this manuscript, the authors used ChatGPT-4o to improve the language and readability of the text. After using this tool, the authors reviewed and edited the content as needed and take full responsibility for the content of the published article.

Data availability

The data supporting the findings of this study are available in the article, Supplementary Information and source data files.

Code Availability

The custom MATLAB R2024b code used for the techno-economic analysis is provided in the Supplementary Information file.

References

1. Anderson ST. Economics, helium, and the US federal helium reserve: summary and outlook. *Nat. Resour. Res.* **27**, 455-477 (2018).
2. Nuttall WJ, Clarke RH, Glowacki BA. Stop squandering helium. *Nature* **485**, 573-575 (2012).
3. Shababa Selim TS. Helium for semiconductors and beyond 2025-2035: market, trends, and forecasts. IDTechEx Ltd. (2025).
4. Helium should be recycled. *Nature* **547**, 6-6 (2017).
5. Hand E. Massive helium fields found in rift zone of Tanzania. *Science* **353**, 109-110 (2016).
6. Oliver B, Bradley JG, Farrar IV H. Helium concentration in the Earth's lower atmosphere. *Geochim. Cosmochim. Acta* **48**, 1759-1767 (1984).
7. Liemberger W, Miltner M, Harasek M. Efficient extraction of helium from natural gas by using hydrogen extraction technology. *Chem. Eng. Trans.* **70**, 865-870 (2018).
8. Zhang Y*, et al.* MOF membranes for gas separations. *Prog. Mater. Sci.* **151**, 101432 (2025).
9. Hao J*, et al.* Scalable synthesis of CO_2-selective porous single-layer graphene membranes. *Nat. Chem. Eng.* 1-11 (2025).
10. Guan J*, et al.* Metal-organic cages improving microporosity in polymeric membrane for superior CO_2 capture. *Sci. Adv.* **11**, eads0583 (2025).
11. Chen X*, et al.* Polyolefin reweaved ultra-micropore membrane for CO_2 capture. *Nat. Commun.* **16**, 282 (2025).
12. Zhou S*, et al.* Asymmetric pore windows in MOF membranes for natural gas valorization.

Nature **606**, 706-712 (2022).
13. Li S*, et al.* Highly porous metal-organic framework glass design and application for gas separation membranes. *Nat. Commun.* **16**, 1622 (2025).
14. Deng Y*, et al.* Flexible ZSM-5 zeolite membrane for high-performance helium separation. *Angew. Chem. Int. Ed.* **64**, e202421285 (2024).
15. Abudaqqa WS, Chaalal O, Chaalal M, Al Hashimi H, Messaoudi F. Review of helium separation from natural gas by membranes. *J. Environ. Chem. Eng.* 116625 (2025).
16. Zhang K*, et al.* ZIF-8 Gel/PIM-1 mixed matrix membranes for enhanced H_2/CH_4 separations. *Chem. Eng. J.* **484**, 149489 (2024).
17. Chen G*, et al.* Solid-solvent processing of ultrathin, highly loaded mixed-matrix membrane for gas separation. *Science* **381**, 1350-1356 (2023).
18. Yu Z, Liu X, Xu X, Tao W, Li Z, Li B. Enhanced selectivity and stability for CO_2 capture through amine-functionalized COFs-based mixed matrix membranes. *Sep. Purif. Technol.* **361**, 131274 (2025).
19. Qin Z*, et al.* Mixed matrix membranes (MMMs) with amine-functionalized ZIF-L for enhanced CO_2 separation performance. *Sep. Purif. Technol.* **344**, 126831 (2024).
20. Zheng W*, et al.* Pore engineering of MOFs through in-situ polymerization of dopamine into the cages to boost gas selective screening of mixed-matrix membranes. *J. Membr. Sci.* **661**, 120882 (2022).
21. Wang Z, Wang D, Zhang S, Hu L, Jin J. Interfacial design of mixed matrix membranes for improved gas separation performance. *Adv. Mater.* **28**, 3399-3405 (2016).
22. Chen W*, et al.* PIM-based mixed-matrix membranes containing MOF-801/ionic liquid nanocomposites for enhanced CO_2 separation performance. *J. Membr. Sci.* **636**, 119581 (2021).
23. Fan S*, et al.* Polymer-MOF network enabling ultrathin coating for post-combustion carbon capture. *Angew. Chem. Int. Ed.* **64**, e202421028 (2024).
24. Yu G*, et al.* Constructing connected paths between UiO-66 and PIM-1 to improve membrane CO_2 separation with crystal-like gas selectivity. *Adv. Mater.* **31**, 1806853 (2019).
25. Wang Z, Tian Y, Fang W, Shrestha BB, Huang M, Jin J. Constructing strong interfacial interactions under mild conditions in MOF-incorporated mixed matrix membranes for gas separation. *ACS Appl. Mater. Interfaces* **13**, 3166-3174 (2021).
26. Lee TH*, et al.* PolyMOF nanoparticles constructed from intrinsically microporous polymer ligand towards scalable composite membranes for CO_2 separation. *Nat. Commun.* **14**, 8330 (2023).
27. He S*, et al.* Symbiosis-inspired de novo synthesis of ultrahigh MOF growth mixed matrix membranes for sustainable carbon capture. *Proc. Natl. Acad. Sci. U.S.A.* **119**, e2114964119 (2021).
28. Wang Z*, et al.* Covalent-linking-enabled superior compatibility of ZIF-8 hybrid membrane for efficient propylene separation. *Adv. Mater.* **34**, 2104606 (2021).
29. Lee TH*, et al.* Interface engineering in MOF/crosslinked polyimide mixed matrix membranes for enhanced propylene/propane separation performance and plasticization

resistance. *J. Membr. Sci.* **667**, 121182 (2023).
30. Deng M*, et al.* High-performance carbon molecular sieve membranes derived from a PPA-cross-linked polyimide precursor for gas separation. *ACS Appl. Mater. Interfaces* **16**, 44927-44937 (2024).
31. Zhao Q*, et al.* Mixed matrix membranes incorporating amino-functionalized ZIF-8-NH_2 in a carboxylic polyimide for molecularly selective gas separation. *J. Membr. Sci.* **693**, 122326 (2024).
32. Jo JH, Lee CO, Ryu GY, Jae H, Roh D, Chi WS. Hierarchical amine-functionalized ZIF-8 mixed-matrix membranes with an engineered interface and transport pathway for efficient gas separation. *ACS Appl. Polym. Mater.* **4**, 6426-6439 (2022).
33. Chaudhari AK, Tan J-C. A mechano-responsive supramolecular metal–organic framework (supraMOF) gel material rich in ZIF-8 nanoplates. *Chem. Commun.* **53**, 8502-8505 (2017).
34. Zhang K*, et al.* Boosting hydrogen transport in mixed matrix membranes through continuous spillover via Pd-functionalized MOF gel networks. *Adv. Funct. Mater.* **35**, 2417186 (2024).
35. Thompson JA, Vaughn JT, Brunelli NA, Koros WJ, Jones CW, Nair S. Mixed-linker zeolitic imidazolate framework mixed-matrix membranes for aggressive CO_2 separation from natural gas. *Microporous Mesoporous Mater.* **192**, 43-51 (2014).
36. Jia Y*, et al.* In-situ interfacial crosslinking of NH_2-MIL-53 and polyimide in MOF-incorporated mixed matrix membranes for efficient H_2 purification. *Fuel* **339**, 126938 (2023).
37. Zheng W, Ding R, Yang K, Dai Y, Yan X, He G. ZIF-8 nanoparticles with tunable size for enhanced CO_2 capture of Pebax based MMMs. *Sep. Purif. Technol.* **214**, 111-119 (2019).
38. Senith Ravishan Fernando J, Asaithambi SS, Maruti Chavan S. Amino-functionalizing Ce-based MOF UiO-66 for enhanced CO_2 adsorption and selectivity. *ChemPlusChem* **89**, e202400107 (2024).
39. Zhao C, Li X, Liu G, Wang X. Selective adsorption of trace CO_2 by immobilized amino acid ionic liquids with ultra-micropores based on amino MOFs. *Sep. Purif. Technol.* **356**, 129742 (2025).
40. Li C, Qi A, Ling Y, Tao Y, Zhang Y-B, Li T. Establishing gas transport highways in MOF-based mixed matrix membranes. *Sci. Adv.* **9**, eadf5087 (2023).
41. Qi A, Li C, Evans JD, Zhao Y, Li T. Self-sorting of interfacial compatibility in MOF-based mixed matrix membranes. *Angew. Chem. Int. Ed.* **63**, e202400474 (2024).
42. Powell CE, Duthie XJ, Kentish SE, Qiao GG, Stevens GW. Reversible diamine cross-linking of polyimide membranes. *J. Membr. Sci.* **291**, 199-209 (2007).
43. Mangindaan DW, Woon NM, Shi GM, Chung TS. P84 polyimide membranes modified by a tripodal amine for enhanced pervaporation dehydration of acetone. *Chem. Eng. Sci.* **122**, 14-23 (2015).
44. Wang H, Paul DR, Chung T-S. Surface modification of polyimide membranes by diethylenetriamine (DETA) vapor for H_2 purification and moisture effect on gas permeation. *J. Membr. Sci.* **430**, 223-233 (2013).

45. Xu S, Liu L, Wang Y. Network cross-linking of polyimide membranes for pervaporation dehydration. *Sep. Purif. Technol.* **185**, 215-226 (2017).
46. Yuan X*, et al.* Performance optimization of imidazole containing copolyimide/functionalized ZIF-8 mixed matrix membrane for gas separations. *J. Membr. Sci.* **644**, 120071 (2022).
47. Lee H*, et al.* Network-nanostructured ZIF-8 to enable percolation for enhanced gas transport. *Adv. Funct. Mater.* **32**, 2207775 (2022).
48. Kanehashi S, Nakagawa T, Nagai K, Duthie X, Kentish S, Stevens G. Effects of carbon dioxide-induced plasticization on the gas transport properties of glassy polyimide membranes. *J. Membr. Sci.* **298**, 147-155 (2007).
49. Fan Y, Yu H, Xu S, Shen Q, Ye H, Li N. Zn (II)-modified imidazole containing polyimide/ZIF-8 mixed matrix membranes for gas separations. *J. Membr. Sci.* **597**, 117775 (2020).
50. Akbari A, Karimi-Sabet J, Ghoreishi SM. Intensification of helium separation from CH_4 and N_2 by size-reduced Cu-BTC particles in Matrimid matrix. *Sep. Purif. Technol.* **251**, 117317 (2020).
51. Zhou Y, He K, Lou Y, Xue J, Wang H. Polyimide-based mixed matrix membranes incorporated with g-C_3N_4 nanosheets for efficient helium enrichment. *Chem. Eng. Sci.* **302**, 120882 (2025).
52. Moghadam F, Omidkhah MR, Vasheghani-Farahani E, Pedram MZ, Dorosti F. The effect of TiO_2 nanoparticles on gas transport properties of Matrimid5218-based mixed matrix membranes. *Sep. Purif. Technol.* **77**, 128-136 (2011).
53. Quader MA, Rufford TE, Smart S. Modeling and cost analysis of helium recovery using combined-membrane process configurations. *Sep. Purif. Technol.* **236**, 116269 (2020).
54. Zhao L, Menzer R, Riensche E, Blum L, Stolten D. Concepts and investment cost analyses of multi-stage membrane systems used in post-combustion processes. *Energy Procedia* **1**, 269-278 (2009).
55. Xu Z, Liu Q, Huang L, Zhu W, Ma X. In-situ crosslinking of a novel conjugated dialkynyl-based polyimide for high performance carbon molecular sieve membrane. *J. Membr. Sci.* **697**, 122572 (2024).
56. Merkel TC, Gupta R, Turk B, Freeman B. Mixed-gas permeation of syngas components in poly (dimethylsiloxane) and poly (1-trimethylsilyl-1-propyne) at elevated temperatures. *J. Membr. Sci.* **191**, 85-94 (2001).

Funding

The authors gratefully acknowledge the financial support from the Open Project Program of State Key Laboratory of Petroleum Pollution Control (Grant No. PPC2023003, recipient S.W.), CNPC Research Institute of Safety and Environmental Technology, the Natural Science Foundation of Changsha, China (kq2402057, recipient S.W.), Guangdong Basic and Applied Basic

Research Foundation (2024A1515011066, recipient S.W.), Hunan Provincial Innovation Foundation For Postgraduate (CX20240454, recipient X.T.) and the Fundamental Research Funds for the Central Universities.

Acknowledgements

The authors thank the Analytical Instrumentation Center of Hunan University for assistance with TEM and DSC measurements.

Author contributions Statement

S.W. and X.M. conceived the concept and revised the manuscript. K.Z. designed and conducted most of the experiments, and drafted the manuscript. H.H. performed gas permeation experiments and conducted techno-economic evaluation. X.T. acquired SEM and TEM images. C.Y. performed PALS measurements. All authors contributed to the manuscript preparation.

Competing Interests Statement

K.Z. and S.W. are inventors on a patent application filed by Hunan University (no. CN202510044823.2) that covers the synthesis and application of the MOF gels described in this paper. The remaining authors declare no competing interests.

Editorial Summary:

Addressing the permeability-selectivity trade-off in helium recovery, the authors engineered MOF gel-crosslinked membranes. Covalent interfacial bonding enables defect-free, ultra-high MOF loadings, yielding exceptional separation performance that pushes beyond conventional upper bounds.

Peer review information: *Nature Communications* thanks Guining Chen, and the other, anonymous, reviewer(s) for their contribution to the peer review of this work. A peer review file is available.